RSC Advances

PAPER

View Article Online
View Journal | View Issue

Cite this: *RSC Adv.*, 2025, **15**, 12028

Preparation of multi-colored carbon dots *via* pH-controlled degradation of wheat bran/*o*-phenylenediamine for Fe^{3+} ion detection†

Wen Xuan Zheng,[ac] Tian Xiang Li,[ac] Yu-hui Xie,[ac] Ya Dong Lv,*[b] De Long Xie*[ac] and Feng Wu *[ac]

Multi-colored carbon dots (CDs) have attracted significant research interest due to their wide range of applications. However, the mechanisms underlying their luminescence and regulation still require further exploration. Herein, blue, green, and orange CDs with different quantum yields were successfully prepared, by changing the thermal degradation behavior of the waste wheat bran/*o*-phenylenediamine *via* adjusting the pH of the acidic hydrothermal conditions. The structure–photoluminescence property relationship of the prepared multi-colored CDs was thoroughly analyzed and discussed, aiming to provide new insights into the luminescence red-shift mechanisms of CDs. It was found that the larger sp^2 domains, higher graphitization of carbon cores, increased graphitic nitrogen, and elevated levels of C=O functional groups contribute to the CDs' lower band gap, resulting in a red-shift of the emission fluorescence. Among them, the elevated levels of C=O functional groups are normally neglected for their contribution in the red-shift of CDs. Additionally, the prepared CDs were explored for their application in monitoring Fe^{3+} content in aquatic environments. A detection limit of 378.76 nM was obtained for the prepared CDs.

Received 31st December 2024
Accepted 4th April 2025

DOI: 10.1039/d4ra09117e

rsc.li/rsc-advances

1. Introduction

In the realm of materials science, carbon element stands out for its diverse orbital hybridization properties, encompassing sp, sp^2, and sp^3.[1,2] Through the coexistence of one or multiple hybridization modalities, carbon forges an extensive array of compounds in nature, unparalleled in its variety.[2] Photoluminescence (PL) carbon dots (CDs), as zero-dimensional nanomaterials with a carbon core skeleton and quasi-spherical morphology, typically exhibit sizes below 10 nm.[3] Since their inception in 2004,[4] CDs have garnered considerable attention and have emerged as a promising material. Extant research reveals that CDs possess numerous advantages, including a broad range of precursor sources,[5] diverse synthesis techniques,[6] tunable fluorescence properties,[7] high thermal and photostability, resistance to photobleaching, exceptional biocompatibility, and low toxicity.[8] These attributes position CDs as potential candidates for numerous applications such as spanning cell imaging,[8] anti-counterfeiting,[9,10] sensing,[7,9] electrodes[11] and corrosion protection.

Color tuning holds significant importance in numerous applications, especially for the bioimaging, information coding and LEDs.[12–14] For example, by modulating the luminescent color of CDs, information encoding and storage can be achieved, offering high-speed, low-power optical storage solutions with exceptional durability.[15] The multicolor fluorescence properties of CDs also facilitate the design of unique luminescent colors and patterns, enabling the development of anti-counterfeiting[9,10,15] labels with distinct identification characteristics. Therefore, Multi-color CDs prepared from different precursors such as spinach,[16] *o*-phenylenediamine,[17–19] graphite rods,[20] L-tyrosine/*o*-phenylenediamine mixture[21] and 4,4-bipyridine/*p*-phenylenediamine[22] have been reported, through concentration or pH regulation.

To tuning the fluorescent properties of CDs, understanding the luminescence mechanism of them is critical. The fluorescence of CDs is a complex process that typically involves multiple luminescent mechanisms.[17] For example, it has been acknowledged that the luminescence of CDs cannot be fully explained by quantum size effects, especially for the CDs with un-ordered crystalline cores.[23] As studied by Zhou *et al.*, they separated the CDs into three different sizes using size exclusion

[a]*Yunnan Provincial Key Laboratory of Energy Saving in Phosphorus Chemical Engineering and New Phosphorus Materials, The Higher Educational Key Laboratory for Phosphorus Chemical Engineering of Yunnan Province, Faculty of Chemical Engineering, Kunming University of Science and Technology, Yunnan 650500, China. E-mail: fengwu@kust.edu.cn; cedlxie@kust.edu.cn*

[b]*College of Polymer Science and Engineering, Sichuan University, Sichuan, 610000, China. E-mail: yadonglv@scu.edu.cn*

[c]*The International Joint Laboratory for Sustainable Polymers of Yunnan Province, Engineering Research Center of Biodegradable Polymers, Educational Commission of Yunnan Province, Kunming, Yunnan, China, 650500*

† Electronic supplementary information (ESI) available. See DOI: https://doi.org/10.1039/d4ra09117e

chromatography to prove that the luminescence behavior of CDs is independent of the size effect.[24] With a deeper understanding of CDs, it is generally believed that the carbon core of CDs includes a hybridized structure of sp^2 and sp^3, and the size of the sp^2 domain in the carbon core significantly affects its luminescent properties. Specifically, an increase in the sp^2 domain decreased the bandgap, leading to a redshift in the fluorescence emission wavelength of CDs.[25,26]

The surface properties of CDs also significantly influence photoluminescence properties.[22] Li *et al.*,. used *m*-phenylenediamine as a precursor and tin(IV) chloride pentahydrate to prepare CDs with numerous reactive $-NH_2$ groups on their surface. By reacting the $-NH_2$ groups with chemicals such as *N*-bromosuccinimide, the function groups of CDs were modified and the color was successfully tuned from green to yellow, orange, and red.[27] This work indicates that the luminescent mechanism of multicolor CDs primarily originates from their excited surface defect band states (also known as surface gap states). Additionally, various theories have been proposed to explain the luminescent properties of CDs, such as molecular states[28] and crosslink-enhanced emission effects.[29] Therefore, through tailoring the bulk and surface properties, CDs with different photoluminescence properties, from blue to red emission have been prepared. Different surface functional stratagem has been adopted. Generally, covalent modifications for CDs include amide coupling, silylation, esterification, sulfonation, and copolymerization, while non-covalent approaches rely on π-interactions, complexation/chelation, and electrostatic interactions. The introduction of functional groups (*e.g.*, amino, carboxyl, hydroxyl) significantly enhances the fluorescence quantum yield, emission tunability, photostability, and analyte complexation efficiency of carbon dots, demonstrating their potential for applications in targeted analyte extraction and controlled drug release.[30] For example, the *p*-phenylenediamine-derived CDs was modified by 4-morpholinoaniline, followed by silica gel column chromatography purification, resulting in an increase in quantum yield from 28.3% to 41.8%;[31] similarly, Maturi *et al.* synthesized red fluorescent CDs *via* a solvothermal method and further modified them through esterification to obtain long-chain surface-functionalized dots (L-RCDs), improving their compatibility and functionality in light-curing printing systems;[32] surface modifications such as N-doping, P-doping, and post-synthesis modifications play a crucial role in tailoring the properties of carbon dots.[33] However, the nature of defects or functional groups and their exact contributions to red-shifted emission are still needed to be explored, to advance the development, and the regulation of luminescence of CDs.

In our previous study, it is discovered that waste biomass undergoes varying thermal decomposition behaviors during hydrothermal treatment, resulting in either the generation of small molecules or the preservation of large macromolecular structures. These differences significantly influence the structure and photoluminescence (PL) properties of the CDs.[34] Building on this finding, we hypothesized that controlling the thermal decomposition of biomass precursors under different pH conditions could produce multi-colored CDs with tunable fluorescence properties. Therefore, a common waste biomass wheat bran, together with theo-phenylenediamine with a conjugated structure, were used to prepare multi-color CDs with tunable fluorescence properties herein. CDs with different colors – orange (o-CDs), green (g-CDs), and blue (b-CDs) were successfully prepared. pH-controlling to tune the PL of CDs has been reported in previous studies.[35–37] Although multi-color carbon dots were obtained through pH regulation, their structures were inconsistent, leading to varying explanations for the mechanism behind their color change. Therefore, a detailed structural analysis is still necessary to clarify the structure–performance relationship of the multi-color carbon dots. In this study, the structure of the CDs was characterized in-depth to understand the relationship between structure and fluorescence properties. Our study aims to not only provide a simple strategy for tuning the fluorescent emission of CDs, but also to advance the understanding of the structural factors influencing their fluorescent properties.

2. Materials and methods

2.1 Materials

o-Phenylenediamine (*o*-PD) (AR grade) was purchased from Aladdin Reagent Co., Ltd., Shanghai. Wheat bran (FG) was purchased from the local farmer industry "Hejiapuzi", Yunnan, China. Concentrated hydrochloric acid (HCl, AR grade) was purchased from Chuandong Chemical Group, China. All chemicals were used as received. The deionized water (DI water) is produced in our lab by using the Millipore milliq Plus ultrapure water system (TKA-Gen Pure).

2.2 Synthesis of carbon dots

To synthesis the carbon dots (CDs), a blend of *o*-phenylenediamine/wheat bran in a weight ratio of 1 : 2 was added into excess distilled water. Wheat bran is used here mainly for its abundance as a low-cost milling by-product and its high protein content, which could facilitate N-doping and enhances the quantum yield of carbon dots. The solution mixture was thoroughly stirred and transferred into a PTFE-lined high-pressure reactor for carbon dots preparation. The reactor was heated in a 120 °C oven for 6 hours. To obtain the CDs with different photoluminescence properties, the pH of the solution was adjusted to 5 and 3 using concentrated hydrochloric acid (HCl). The choice of hydrochloric acid (HCl) for pH adjustment was based on the need to minimize exogenous heteroatom interference while maintaining effective hydrolysis. As demonstrated by Qiu *et al.*,[38] inorganic acids (*e.g.*, HNO_3, H_2SO_4) enhance cellulose degradation but introduce nitrogen or sulfur residues into the carbon matrix, which may artificially elevate quantum yields or obscure the intrinsic properties of the wheat bran precursor. Organic acids (*e.g.*, formic acid) similarly risk altering surface functional group profiles. In contrast, HCl provides H^+ ions for proton-assisted hydrolysis without introducing non-volatile anions, thereby preserving the biomass-derived carbon core's elemental fidelity. This aligns with our

study's focus on elucidating the intrinsic mechanisms of agricultural waste conversion to multicolor CDs.

After the reaction was completed and the reactor had cooled, the solution was centrifuged at 10 000 rpm for 30 minutes to remove any large insoluble particles. The supernatant was collected and filtered through a 0.22 μm membrane filter. The filtered solution was further dialyzed using a 500 Da MWCO ultrafiltration membrane for 24 hours to remove any unreacted impurities. Finally, the dialyzed solution was dried (*via* freeze-drying) to obtain the carbon dots powder. The schematic of the CDs preparation was showed in Fig. S1.† The prepared carbon quantum dots were stored in a refrigerator at 4 °C for subsequent testing. Finally, orange (named as o-CDs), green (g-CDs) and blue (b-CDs) CDs were successfully prepared at pH = 7, 5, and 3.

2.3 Testing and characterization

The UV-vis properties of the prepared CDs were assessed through UV-Vis absorption spectroscopy (Shimadzu UV-2250, Japan), with measurements taken over the range of 200 to 700 nm and analyzed using the "M. Wave Professional" software. Fluorescence emission spectra (PL) were recorded using a Shimadzu RF-6000 PC spectrophotometer (Japan), with readings collected at 1 nm intervals between 200 and 700 nm. The fluorescence lifetime of the CDs/H_2O solution was evaluated using an Edinburgh FLS1000 instrument (UK), employing a 1 cm quartz fluorescence cuvette and excitation at 375 nm from a picosecond pulsed LED. Throughout these tests, DI water was served as the solvent.

The quantum yield (QY) of the CDs was determined *via* the relative method, using quinine sulfate dissolved in a 0.05 M sulfuric acid solution as a reference, which has a QY of 55% at an excitation wavelength of 350 nm. The calculation of the QY was carried out as eqn (1).[39]

$$\Phi_x = \Phi_s \cdot \frac{F_x}{F_s} \cdot \frac{A_s}{A_x} \cdot \frac{\eta_x}{\eta_s} \quad (1)$$

In the equation, Φ_s and Φ_x represent the QY of the standard and the CDs, respectively, while F, A, and η refer to fluorescence intensity, absorbance, and the refractive index of the solvent at the excitation wavelength. F is derived from the area S of the fluorescence emission peak, which falls between 480 and 620 nm.

The surface chemical composition of the CDs was examined using X-ray photoelectron spectroscopy (XPS) with a Thermo Kalpna (Thermo Scientific, USA) system, utilizing a monochromatic Al Kα X-ray source with a photon energy of 1486.6 eV, operating at 6 mA × 12 kV.

The Fourier Transform Infrared Spectroscopy (FTIR) of the synthesized CDs were carried out in transmission mode, with a wavelength range of 400 to 4000 cm^{-1} and a resolution of 4 cm^{-1} (FTIR, Nicolet 5700). The CDs were each mixed with KBr powder and pressed into disks for the test.

The Transmission Electron Microscopy (TEM) images of the CDs was visualized through high-resolution TEM (HRTEM) using a JEM-2100F microscope (JEOL, Japan). To calculate the particle size distribution, at least 50 particles were statistic analyzed with the help of Nano Measurer 1.2 software.

The internal structure of the CDs was characterized by Raman spectroscopy and X-ray diffraction (XRD). Raman spectra were recorded using a Lab Ram HR Evolution spectrometer (HORIBA Scientific, France). The scanning was from 50 to 3000 cm^{-1}, the excitation source was a 532 nm laser. For XRD analysis, dried CD powder samples were analyzed with an Anton Paar XRDynamic500 instrument, using a Cu Kα source at 30 kV and 10 mA, scanning from 5° to 90° with a 0.1° step size and a 2-second integration time.

3. Results and discussions

3.1 Optical properties of o-CDs, g-CDs, b-CDs

Using wheat bran and *o*-phenylenediamine as carbon sources, the hydrothermal synthesis of o-CDs, g-CDs, and b-CDs was carried out under different pH. To delve into the microscopic morphological attributes of o-CDs, g-CDs, and b-CDs, a transmission electron microscopy (TEM) analysis was conducted. As shown in Fig. 1a, the o-CDs, g-CDs, and b-CDs in aqueous exhibited quasi-spherical morphologies with a uniform distribution. To quantify these observations, a statistical analysis of the TEM images was performed, yielding the particle size distributions as depicted in Fig. 1b. The mean particle size and standard deviation (SD) were o-CD: 5.55 ± 0.78 nm; g-CD: 2.89 ± 0.35 nm; and b-CD: 1.87 ± 0.21 nm, respectively. Notably, all three CDs exhibit particle sizes smaller than 10 nm that meets the definition of CDs, indicating the successful synthesis of CDs. However, it is discernible that the particle size of the CDs gradually decreased with increasing pH values, *i.e.*, the size of o-CDs > g-CDs > b-CDs, by using the same molecular weight cut-off membranes. It means that the size of CDs is depended on the pH. Dai and his co-workers also used pH to turn the size of the CDs, but their study found that the lower pH, the larger size of the CDs.[35] The difference is suggested to be resulted from the different reaction of the precursors under different pH condition. Under acidic conditions, the hydrolysis of lignocellulosic biomass (*e.g.*, wheat bran) will be significantly facilitated and smaller molecular fragments will be produced as precursors for carbonation,[38,40,41] which confirms our observation in the TEM (Fig. 1) of a decrease in CD size with increasing acidity. And as the acidity of the reaction increases, the oxidized group (C═O at 1600 cm^{-1}) and (C═C at 1520 cm^{-1}) peaks in the FTIR spectra of CDs (Fig. 3a) diminish, which suggests that the polymerized chain is broken down into more fragmented monomers. Furthermore, as confirmed by XPS C1s analysis (Fig. 4), these fragments were carbonized to form CDs with compact sp^2 structural domains. We propose that acidic conditions may promote hydrolysis of the precursor, potentially fragmenting carbohydrate and protein chains into smaller segments. These fragments are further carbonized, resulting in CDs with reduced dimensions, as supported by TEM analysis.

Further optical characterization *via* UV-visible spectroscopy revealed variations in the absorption peaks of the three types of CDs. Under 365 nm UV illumination, the solutions exhibited distinct orange, green, and blue fluorescence, respectively, as

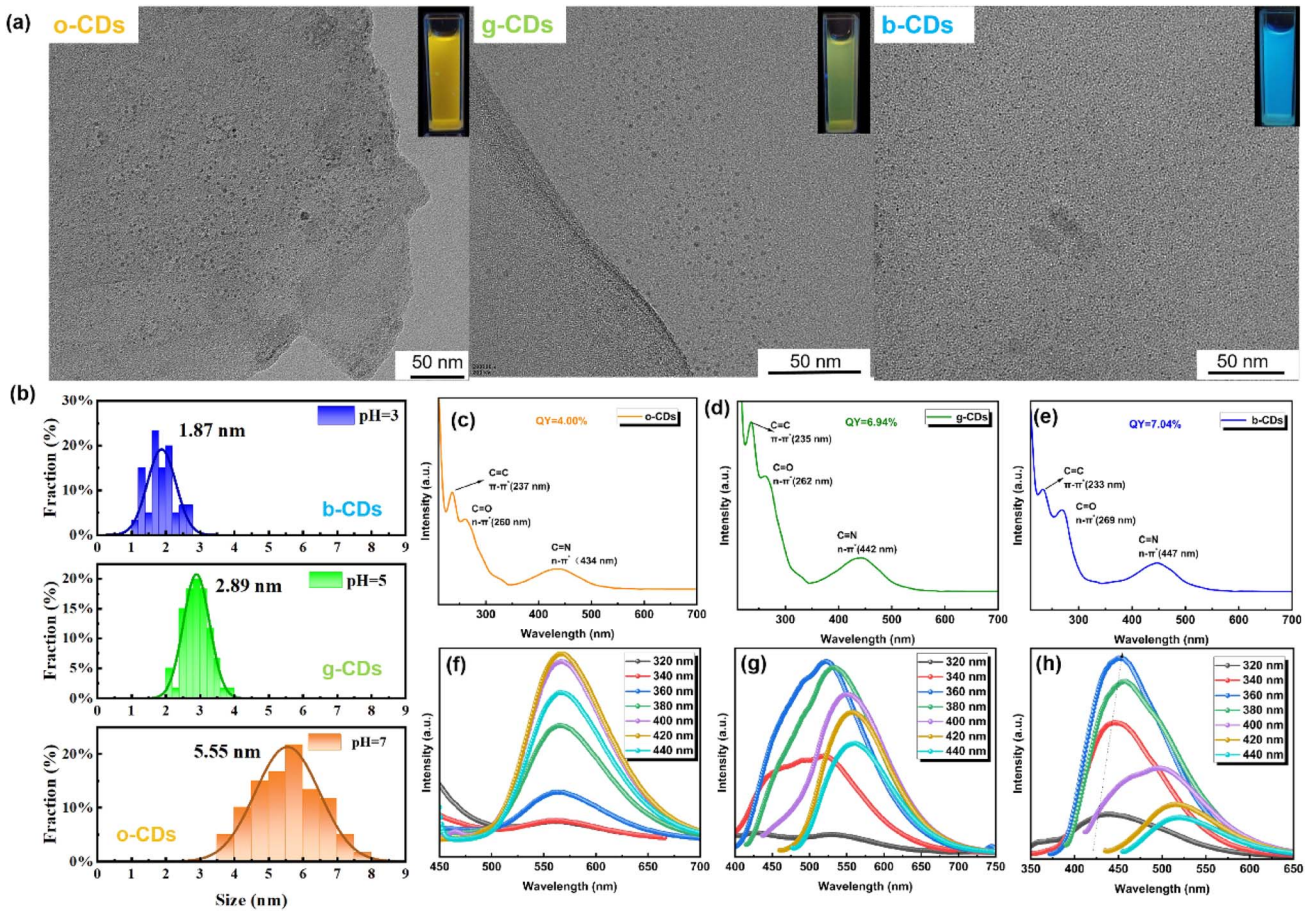

Fig. 1 (a) High-resolution TEM of o-CDs, g-CDs, and b-CDs (inset shows fluorescence photos illuminated by a 365-nm UV lamp); (b) particle size distributions of o-CDs, g-CDs and b-CDs; (c–e) UV-visible absorption spectra of o-CDs (c), g-CDs(d), and b-CDs (e); and (f–h) fluorescence spectra of o-CDs (f), g-CDs (g), and b-CDs (h).

showed in Fig. 1a. As depicted in Fig. 1c, the absorption peaks corresponding to π–π* transitions of C=C/C=N in the aromatic carbon clusters were observed at 237 nm (o-CDs), 235 nm (g-CDs), and 233 nm (b-CDs). While the absorption attributed to n–π* transitions of C=O/C=N bonds were noted at 260 nm for o-CDs, 262 nm for g-CDs, and 269 nm for b-CDs.[34] Notably, all three CDs exhibited additional absorption peaks at longer wavelengths, located at 434 nm (o-CDs), 442 nm (g-CDs), and 447 nm (b-CDs), attributed to the surface conjugated groups attached to the edges of inner cores.[35] While the π–π* transition absorption peaks exhibited a minor blue shift, there were a distinct red shift in the absorption peaks related to n–π* transitions of the surface conjugated groups from o-CDs to b-CDs. This suggests that the energy level of the π–π* transition increases, while the energy level of the n–π* transition decreases. Typically, as the size of the sp^2 domain in the carbon core decreases, a blue shift in the absorption peaks is observed due to the increased energy gap in the inner core,[18] consistent with our π–π* transitions. However, for the n–π* transitions involving surface groups, it is suggested that a decrease in pH would promote dehydration and carbonization of the precursors, thereby increasing the number of functional groups and enhancing the degree of oxidation. Additionally, higher pH would facilitate the formation of CDs with larger conjugated domains and narrower energy gaps,[42] making n–π* transitions more favorable.

The fluorescence emission spectra of the three CDs were showed in Fig. 1d–f. The photoluminescence (PL) emission peaks are located at 565 nm for o-CDs, 521 nm for g-CDs, and 450 nm for b-CDs, which are corresponding to their emission colors in Fig. 1a. But it is interesting to find that the emission of o-CDs is independent of excitation wavelength, while the other two CDs, *i.e.*, g-CDs and b-CDs is wavelength dependent. The fluorescence emission of the g-CDs and b-CDs exhibited typical red-shift with increasing excitation wavelength from 360 to 440 nm. The o-CDs exhibit excitation-independent emission due to more uniform or homogeneously distributed emission centers. It has relatively consistent electronic environments and do not show significant changes in PL spectra with varying excitation wavelengths. This can be attributed to its relatively larger sp^2 domain size, less surface defects and functional groups when hydrothermal treated at pH = 7. It is known that smaller CDs can have size-dependent energy levels that vary with the excitation wavelength, leading to different emission spectra due to quantum confinement effects.[7,43]

To better illustrate the relationship between the structures such as the sp^2 domain structure and surface groups, and the PL properties of the CDs, more detailed analysis of the morphology and structures of the three different CDs are carried out.

3.2 Morphological and structural characterization of o-CDs, g-CDs, b-CDs

3.2.1 Crystal structure and graphitization degree. High-resolution TEM (HTEM) imaging in Fig. 2a revealed that the lattice spacing of the three CDs was approximately 0.21 nm, which is corresponding to the [100] crystal plane of graphite carbon lattice.[44] The sixfold symmetric fast Fourier transform (FFT) patterns of the lattice is also given in Fig. 2a, along with the identical well-resolved lattice fringes. It seems that b-CDs present a more homogeneous crystal structure while the crystal structure of o-CDs is more oriented. Specifically, an augmentation in sp^2 domains enlarges the rigid areas within the CDs' structure, subsequently leading to an expansion in particle size from b-CDs to o-CDs. Concurrently, the enhancement of sp^2 domains results in a narrowing of the CDs' bandgap, thereby inducing longer fluorescence emission wavelength of o-CDs (ref-shift), which is identical to the optical properties discussion.

The Raman spectra in Fig. 2b was used to explore the graphitization degree of the CDs. The G band, which is corresponding to the E_{2g} symmetry phonon at the Brillouin zone center due to the in-plane vibration of sp^2-bonded carbon atoms,[45] shifts to lower wavenumbers with increasing pH (from o-CDs to b-CDs). The D band, which is associated with the breathing mode of sp^2 rings and is indicative of disorder in the material,[46] does not exhibit a similar shift. This suggests that while the electronic structure or bonding environment of the sp^2 carbon changes with varying pH, the defect density or overall structure remains largely unaffected. Several factors, including strain, doping, graphitization, the size of sp^2 domains, or quantum confinement effects, could contribute to this observed shift.

Given that the strain applied and the doping in the three CDs are identical, the shift of the G band can be primarily attributed to differences in graphitization and the size of sp^2 domains. The HRTEM images reveal that the sp^2 domains of o-CDs are larger than those of b-CDs. As the size of CDs increases, quantum confinement effects become less significant, and the vibrational energy levels become less discrete.[47] Meanwhile, larger CDs behave more like bulk graphitic carbon, where the phonon modes are more constrained. This results in stiffer vibrations of the sp^2 carbon atoms, leading to a blue shift (higher wavenumbers) in the G band.

In addition to size reduction, the graphitization or increased ordering within the sp^2 domains significantly affects the Raman G band, which corresponds to the in-plane stretching vibrations of sp^2 carbon atoms. The degree of graphitization was determined using the $I(D)/I(G)$ ratio, as presented in Table 1. A gradual decrease in the $I(D)/I(G)$ ratio from b-CDs to o-CDs indicates a higher degree of graphitization (a more ordered carbon structures) within the CDs' internal structure. The increased graphitization of o-CDs explains the blue shift of the G band (toward higher wavenumbers), as vibrational modes in graphitic carbon are less disrupted by disorder.[48] Consequently, as the structure becomes more ordered (graphitized), the G band reflects more rigid vibrational modes, resulting in the observed blue shift.

The XRD spectrum, shown in Fig. 2c, reveals the crystalline core structure of the CDs. All three CDs exhibited peaks at 21°,

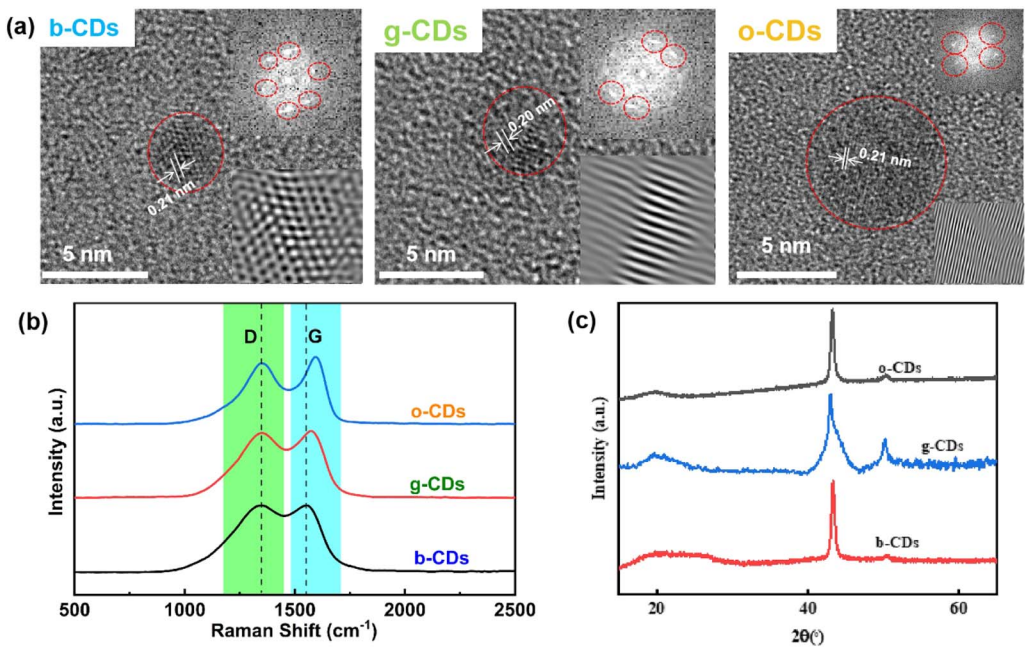

Fig. 2 The crystal structure and graphitization of the CDs: (a) HRTEM of the CDs; (b) the Raman spectra of the CDs; (c) the XRD of the CDs.

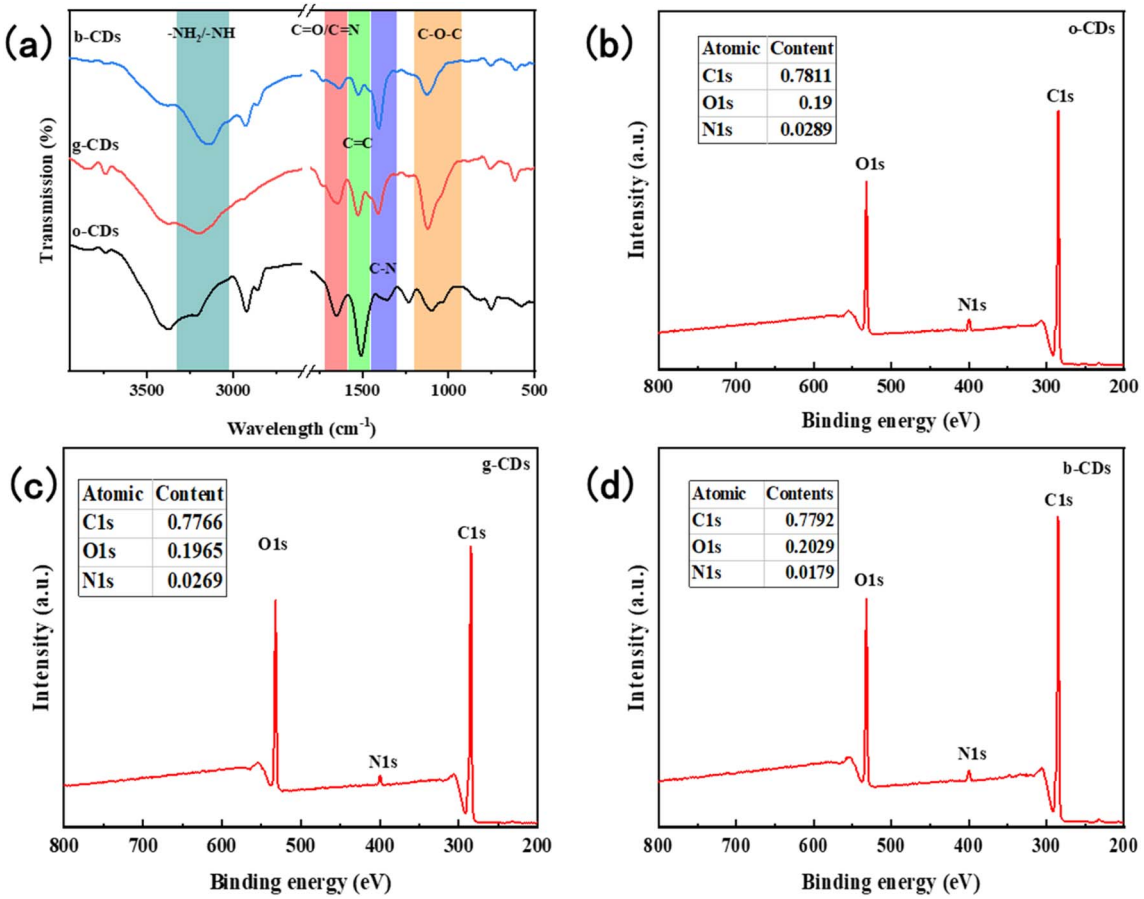

Fig. 3 (a) The Fourier transform infrared spectra of o-CDs, g-CDs, and b-CDs and (b) full XPS spectra of o-CDs (b), g-CDs (c), and b-CDs (d).

43°, and 50°, though the shape and intensity of these peaks varied significantly. The *d*-spacings were calculated from the XRD spectrum using Bragg's Law, corresponding to 0.44, 0.21, and 0.18 nm, respectively. The prominent peak at 43° is attributed to the carbon core with a *d*-spacing of 0.21 nm, which aligns with the HRTEM observations. The weak peaks at 21° indicate the presence of non-ideally arranged graphite-like structures, such as the [002] plane in graphite.[49] The higher intensity and sharpness of the peaks, particularly at 43°, indicate that the o-CDs exhibit a significantly higher degree of crystallinity compared to the g-CDs and b-CDs. This observation is consistent with the degree of graphitization calculated from the Raman spectra, where o-CDs exhibit the highest degree of graphitization.

Based on the HRTEM, Raman, and XRD analyses, it was found that the addition of acid during the reaction process more thoroughly disrupts the cellular structure of wheat bran, leading to a more disordered conjugated structure in the prepared CDs. As a result, the sp^2 domains and graphitization of the carbon cores are reduced, along with the particle size. The weakening of sp^2 domains and graphitization broadens the CDs' bandgap, causing a blue-shift in the fluorescence emission spectra. This explains why, as the pH increases, the carbon dots gradually shift from emitting orange to blue light.

3.2.2 Composition and surface chemistry. The surface groups present in CDs are characterized by FTIR and XPS as showed in Fig. 3. The FTIR peak at 1507 cm^{-1} corresponds to the C=C absorption, which is characteristic of conjugated sp^2 domains. A meticulous examination of the IR spectra reveals a progressive decrement in the C=C peak intensity from o-CDs to b-CDs. This decrement signifies a decrease in the abundance of conjugated structures within the CDs, resulting in a diminished sp^2 domain size, as discussed previously.

Furthermore, the FTIR results show that the surface functional group of the three types of CDs are significant differences. Notably, during the progression from o-CDs to b-CDs, a conspicuous enhancement in the intensity of the $\nu_{(CN)}$ at 1403 cm^{-1} (C–N/C=N) and the $\nu_{(NH)}$ at 3157 cm^{-1} (corresponding to $-NH_2$/–NH vibration) was observed, accompanied by a gradual attenuation in the C=N absorption peak at 1350 cm^{-1}. Meanwhile, the $\nu_{(NH)}$ at 3157 cm^{-1} shifts to lower wavenumbers along with the transition from o-CDs to b-CDs. All those evolutions indicate that the N-containing groups on the surface of the CDs have been changed during the transition from o-CDs to b-CDs, which will be further discussed by XPS. We also find that the peaks at 1235 cm^{-1} corresponding to the aryl –O stretching and 3370 corresponding to the –OH stretching gradually disappeared with the transition from o-CDs to b-

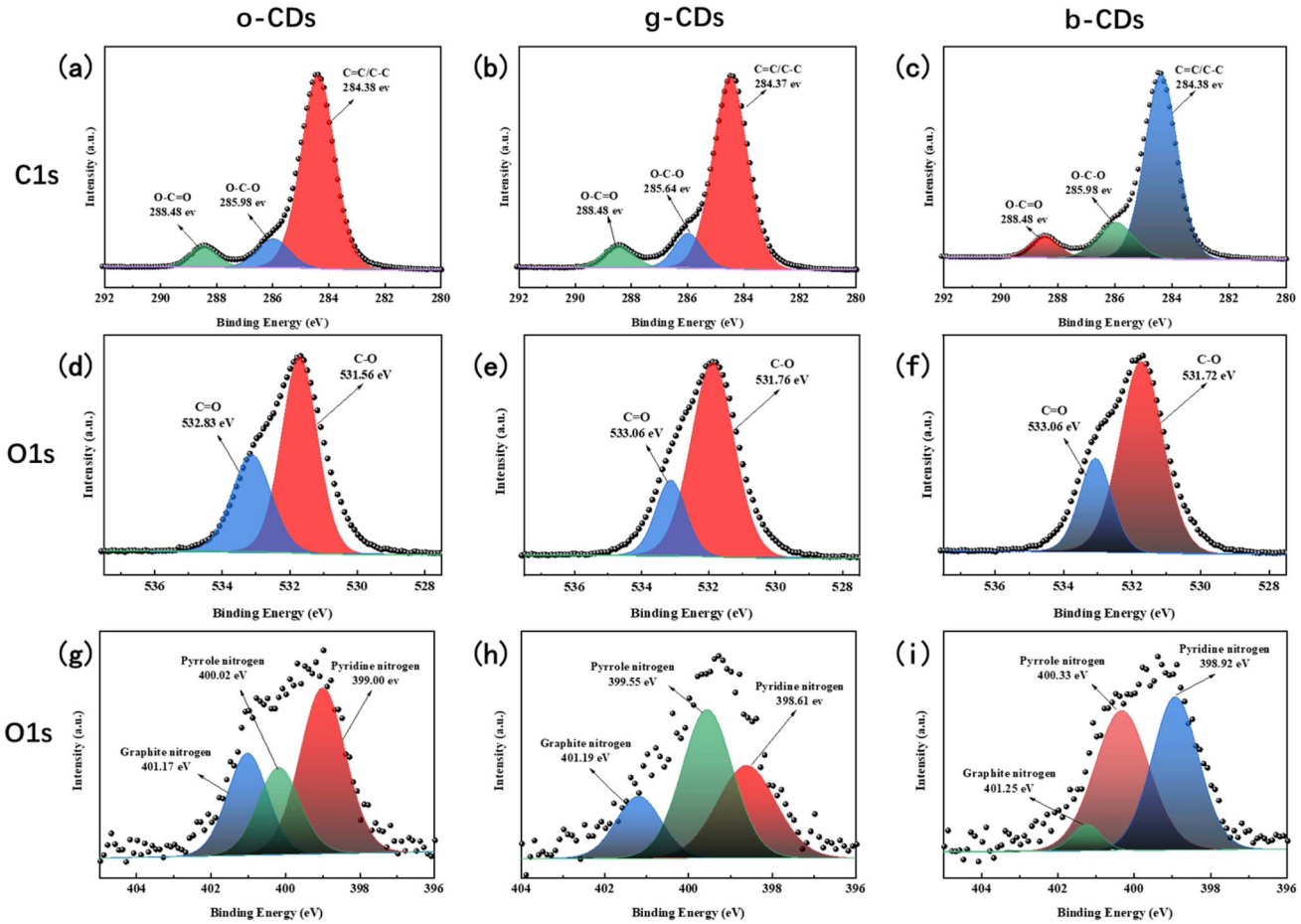

Fig. 4 The C1s profiles of o-CDs (a), g-CDs (b) and b-CDs (c), the O1s profiles of o-CDs(d), g-CDs (e) and b-CDs (f), and the N1s profiles of o-CDs (g), g-CDs (h) and b-CDs (i).

CDs, indicating the oxygen-containing functional groups such as C–O or C═O are also changed. To further clarify the changes in these functional groups, XPS spectra is carried out.

Fig. 4b–d present the full XPS spectra of o-CDs, g-CDs, and b-CDs, respectively. As evident from the spectra, all three CDs exhibit characteristic peaks for C1s (285 eV), N1s (400 eV), and O1s (531 eV), with minor variations in their respective concentrations. As detailed in Table 2, a significant increase in the C/N ratio is observed as the CDs transition from o-CDs to b-CDs, while the C/O ratio gradually reduced, which is consistent to the FTIR analysis. The content of N is relatively high in o-CDs compared to that of g-CDs and b-CDs. O exists both in the carbon core skeleton and on the surface of the carbon core, primarily in the form of surface oxygen-containing functional groups, where the content of –COOH of o-CDs is higher than that in g-CDs and b-CDs as analyzed by the high-resolution X-ray photoelectron spectroscopy (XPS) in Fig. 4. The graphitic nitrogen content gradually decreases from o-CDs (26.76 at%) to b-CDs (5.02 at%) while the oxygen content increases (Table 2), which is associated with the emission redshift. This is in agreement with previous findings that higher graphitic nitrogen (N-doped sp^2 domain) and carbonyl (C═O) decrease the band gap.[50]

The high-resolution XPS spectra for carbon revealed three distinct peaks common to all three types of CDs: the peak near 284.2 eV corresponds to sp^2/sp^3 hybrid carbon (C–C/C═C), the peak around 285.9 eV indicates the presence of carbon–oxygen bonds (C–O), and the peak at 288.4 eV represents carbonyl carbon (C═O). For oxygen (O1s), two peaks were identified: one near 533.3 eV, corresponding to C═O, and another around 531.4 eV, corresponding to C–O. These peaks reflect the presence of carbon-oxygen double and single bonds, respectively, on the surface of the CDs.

Table 2 and Fig. 5 show that as the CDs transition from o-CDs to b-CDs, the content of C═O decreases while the content of C–O increases. This indicates a transformation of surface oxygen-containing functional groups from C═O to C–O, which in turn affects the optical properties of the CDs. The C═O groups enhance the conjugation of π-electrons, leading to a red shift in the fluorescence emission. Therefore, the conversion from C═O to C–O is associated with a blue shift in the fluorescence.[5]

The nitrogen forms in the CDs—graphitic nitrogen, pyrrolic nitrogen, and pyridinic nitrogen—were also characterized, with their relative abundances varying among the different CDs, as shown in Fig. 5b. During the transition from o-CDs to g-CDs,

Table 1 The results obtained from Raman spectra

	o-CDs		g-CDs		b-CDs	
Area of peak	I(D)	I(G)	I(D)	I(G)	I(D)	I(G)
	1744123.61	1403680.85	1760002.69	1401869.87	2370597.95	1761163.52
I(D)/I(G)	1.24		1.26		1.35	

Table 2 The results were analyzed by XPS data

	Area (%)									
	C1s			O1s		N1s				
CDs	C=C/C–C	O–C–O	O–C=O	C–O	C=O	Pyridine N	Pyrrole N	Graphite N	C/O	C/N
o-CDs	81.31	11.36	7.33	55.91	44.09	49.37	23.88	26.76	4.11	27.03
g-CDs	66.04	25.03	8.93	69.57	30.43	34.45	47.80	17.75	3.95	28.87
b-CDs	75.90	16.21	7.88	73.46	26.54	46.21	48.77	5.02	3.84	43.53

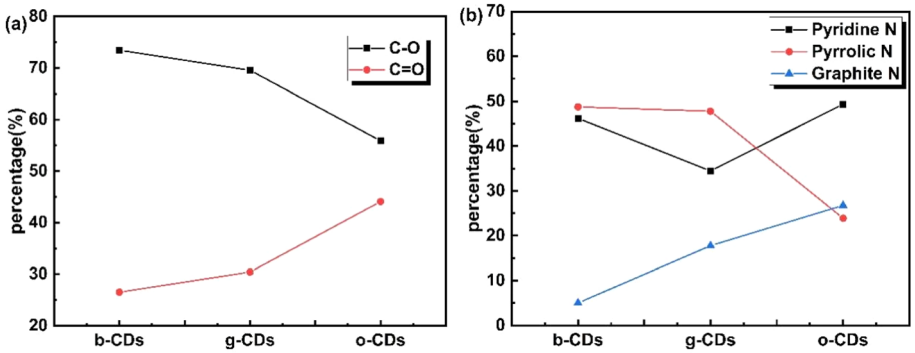

Fig. 5 (a) Comparison of C–O and C=O contents of o-CDS, g-CDs and b-CDs, (b) Comparison of contents of pyridine N, pyrrole N and graphite N in o-CDS, g-CDs and b-CDs.

and further to b-CDs, the content of graphitic nitrogen decreases, pyrrolic nitrogen increases, and pyridinic nitrogen first decreases then increases. These observations suggest that graphitic nitrogen is mainly converted to pyrrolic nitrogen during the transformation from o-CDs to g-CDs. As the transition continues to b-CDs, pyrrolic nitrogen further transforms into pyridinic nitrogen, resulting in a reduction of graphitic nitrogen in the carbon structure. While XPS reveals the overall elemental composition, advanced techniques such as EELS could further resolve core–shell elemental gradients. Nevertheless, our FTIR and XPS results collectively support the proposed luminescence mechanism dominated by nitrogen doping and oxidation state modulation.

Graphitic nitrogen plays a key role in determining the fluorescence properties of CDs, particularly in causing a redshift in emission due to its electron-doping effect, which narrows the electronic band gap.[35] Therefore, the o-CDs with highest graphitic N contents exhibits longest wavelength PL, which is identical to the previous studies.[35] In the case of b-CDs with highest QY, the proportion of graphitic N was the lowest with edge nitrogen species such as pyridine N and pyrrole N becoming dominant. It means that the existence of edge nitrogen probably moderately augments the fluorescence quantum yield of CDs, yet it does not narrow the band gap.

The fluorescence lifetime of the three CDs was calculated by fitting the fluorescence intensity curves shown in Fig. 6. The curves were successfully fitted using a mono-exponential decay function,[51] with a high correlation coefficient (R^2 > 0.99). This mono-exponential fitting suggests that the CDs possess a single fluorescence (FL) origin, likely due to their uniform size distribution and emission traps.[52,53] The fluorescence lifetimes of the o-CDs, g-CDs, and b-CDs were determined to be 1.88 ns, 1.10 ns, and 1.73 ns, respectively.

Typically, the lifetimes of CDs are associated with their core and surface states.[54] In semiconductor nanocrystals, it is generally observed that larger crystal sizes correspond to shorter excitonic photoluminescence (PL) lifetimes.[55] However, the o-CDs, despite having the largest crystal size, exhibit the longest lifetime, indicating that surface states significantly influence the lifetime of the CDs but not the crystal size. In a study by Hola *et al.*, it was found that low-energy radiative recombination (red-shifted emission) led to longer lifetimes in CDs, which can

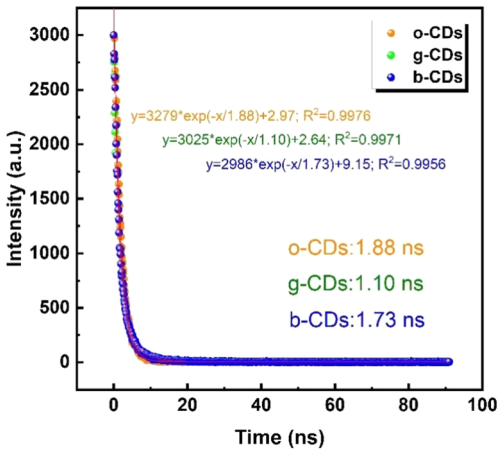

Fig. 6 Fluorescence lifetimes of o-CDs, g-CDs, and b-CDs were tested and calculated at an excitation wavelength of 375 nm.

be attributed to the prolonged charge carrier relaxation to lower-lying energy levels.[54] Consequently, the o-CDs, which have the longest emission wavelengths, also exhibit the longest lifetime.

The shortest fluorescence lifetime of the g-CDs is suggested to result from the high crystal defects and the highest oxygen-containing groups on their surface, as revealed by the XRD and XPS results. The XPS analysis shows that the C=C/C–C content in the g-CDs is the lowest among the three, while the O–C–O content is the highest. The XRD results further indicate that the g-CDs have more crystal defects, evidenced by a broader peak at 43°, which is associated with either carbonyl groups or epoxide bonding between the lattices.

To isolate the role of *o*-phenylenediamine (*o*-PD) in fluorescence modulation, we synthesized CDs using raw wheat bran without *o*-PD under identical hydrothermal conditions (pH = 7). As shown in Fig. 7a, the *o*-PD-free CDs exhibit a unimodal size distribution centered at 3.93 ± 1.50 nm (TEM image in Fig. 7c). However, their photoluminescence (PL) spectra differ significantly. Upon 320 nm excitation (Fig. 7b), the *o*-PD-free CDs emit a weak blue fluorescence with a broad peak at 440 nm, while *o*-PD-containing CDs (*o*-CDs) under the same pH show enhanced orange emission at 560 nm. This contrast highlights that *o*-PD promotes nitrogen doping (as evidenced by XPS in Fig. 4). Furthermore, the absence of multicolor emission in raw wheat bran CDs underscores *o*-PD's critical role in creating tunable bandgaps *via* heteroatom incorporation.

3.3 Mechanism discussion behind the optical properties

All three CDs were synthesized using bran and o-phenylenediamine in a high-pressure hydrothermal reactor under identical reaction conditions, with pH being the only variable: unadjusted (7.5–8.2), weakly acidic (5.5–6.0), and strongly acidic (2.5–3.0). The wheat bran comprises approximately 12% water, 18% protein, 3.5% fat and 56% carbohydrates,[56] which experience different structure evolution in different pH condition. Degradation products, mainly the glucose, oligomers, sugar monomers, and amino acids, noticeably begin to increase at more severe hydrothermal treatment conditions,[57,58] such as the strongly acidic environment. This means that more small molecules participate in the formation of CDs when decreasing the pH, resulting in less conjugated sp^2 domains, lower graphitization of carbon cores, and higher surface oxidation, which is identical to our previous studies on the hydrothermal of different biomass.[34] Meanwhile, the graphitic N contents are also reduced with the structures of o-PD and wheat bran being destroyed under acidic treatment.

The increased graphitization of CDs from blue to orange could be related to the stepwise evolution of the core structure of carbon dots under acidic hydrothermal conditions. Initially, precursor depolymerization occurs, where proton-catalyzed degradation breaks down cellulose and proteins in wheat bran into small molecular fragments. This is followed by carbon core nucleation, where these small molecules undergo dehydration and condensation to form initial sp^2 domains. Subsequently, graphitization and expansion take place, driven by high temperatures (180 °C), leading to the formation of more ordered graphite-like microcrystals through aryl ring planar stacking and π–π interactions. A more severe acidic environment (lower pH) may destroy the order of the carbon core in this process, reducing its degree of graphitization. Finally, surface passivation occurs, where residual oxygen- and nitrogen-containing functional groups (*e.g.*, C=O, $-NH_2$) are anchored

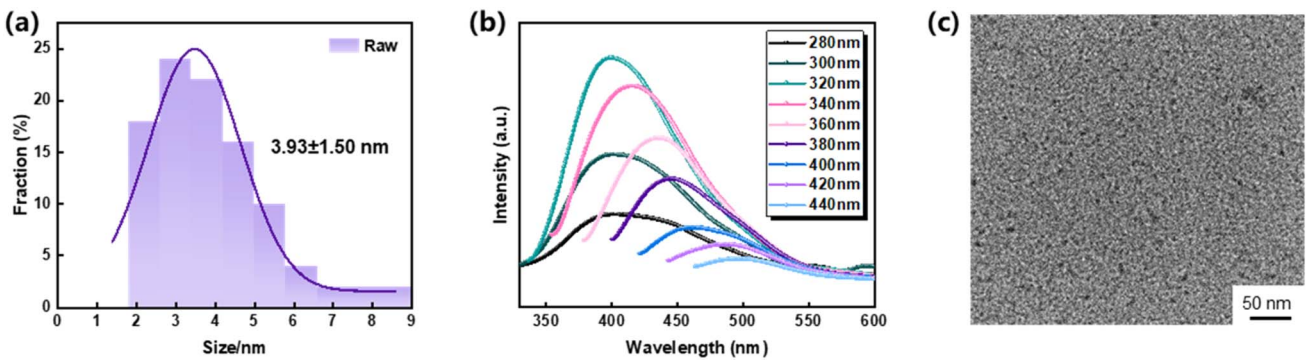

Fig. 7 Particle size distribution of free-*o*-PD-CDs (a) fluorescence emission spectra (b) and TEM (c).

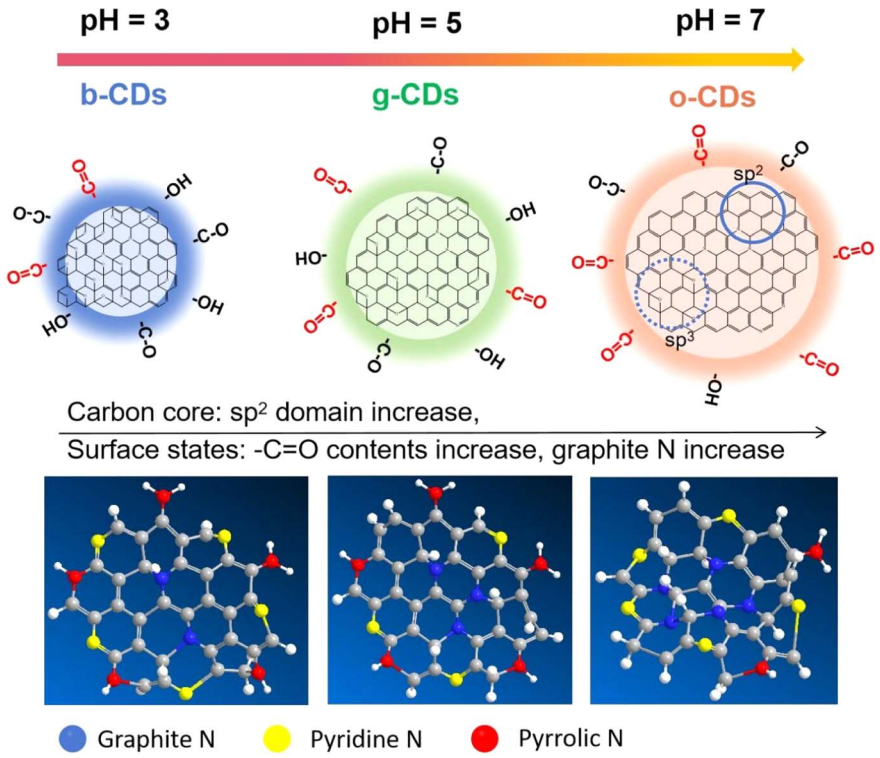

Fig. 8 Schematic of the multi-color carbon dots developed under different pH conditions and their structure evolution.

at the edges of the nucleus, regulating the surface state energy distribution.

Our studies confirm that the b-CDs obtained under low pH conditions possess smaller sp^2 domains and a lower degree of graphitization. Beyond these factors, detailed characterization reveals that as the fluorescence shifts from blue (b-CDs) to orange (o-CDs), there is an increase in sp^2 conjugation within the carbon cores, and N-doping transitions to more stable graphitic nitrogen forms. Furthermore, variations in oxygen content and its bonding types on the CDs' surfaces also contribute to the fluorescence shift. Although the overall oxygen content decreases from b-CDs to o-CDs, the percentage of oxygen involved in carbon-oxygen double bonds (C═O) increases, enhancing π-electron conjugation and causing a redshift, as showed in Fig. 8. Moreover, we conducted hydrothermal processing of CDs at different temperatures (120 °C, 150 °C, and 180 °C). The resulting CDs displayed a blue-shift with increasing temperature (Fig. S2†), likely due to the

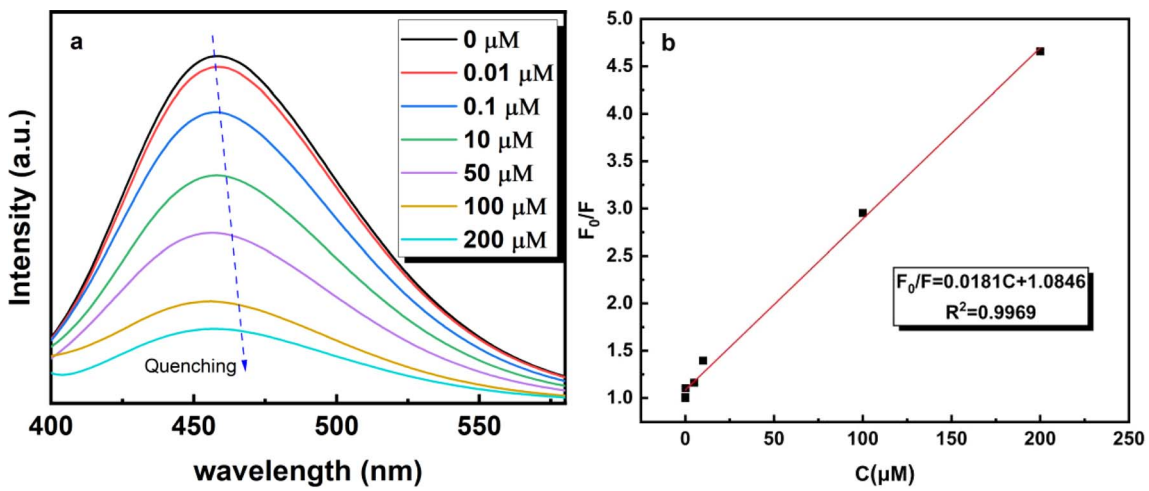

Fig. 9 (a) Fluorescence emission spectra of b-CDs in Fe^{3+} solutions with varying concentrations from 0.01 to 200 μM. (b) Fitting curve of F_0/F as a function of Fe^{3+} ion concentration for b-CDs.

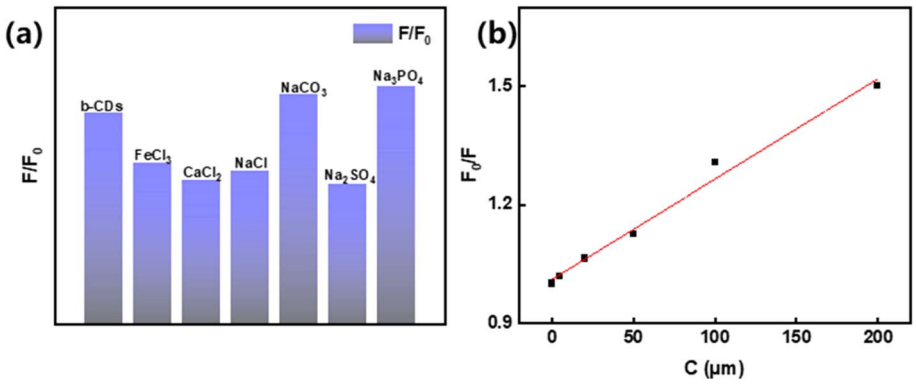

Fig. 10 F/F_0 of Fe^{3+} detected at 100 μM L^{-1} in 200-fold disturbed water (a); variation of Fe^{3+} in the concentration gradient detected in natural water (b).

more extensive degradation of wheat bran at higher temperatures. This finding further supports our earlier hypothesis that smaller molecules are increasingly involved in CD formation under more intense thermal degradation conditions.

3.4 Ion detection application of b-CDs

To assess the sensitivity of CDs for the optical detection of Fe^{3+}, a series of Fe^{3+} solutions with concentrations ranging from 0.01 to 200 μM are prepared, using b-CDs, which possess the highest quantum yield (7.04%), as a model (Fig. 9). *Via* defining the fluorescence intensity of the b-CDs solution as F_0, and the fluorescence intensity of the b-CDs solution in the presence of Fe^{3+} ions as F, the ratio F_0/F is plotted against the concentration of Fe^{3+} ions (C_Fe^{3+}). As shown in Fig. 8, the F_0/F increases with increasing Fe^{3+} concentration, indicating a reduction in the fluorescence intensity of the b-CDs solution. The quenching effect of Fe^{3+} on b-CDs exhibites a good linear correlation (the correlation coefficient (R^2) was 0.9969) within the concentration range of 0.01 to 200 μM. It is predicted that the detection limit of the CDs for Fe^{3+} ions is 378.76 nM from the linear relationship.

To evaluate the practical potential of b-CDs for the detection of Fe^{3+}, the interference effects of common co-existing ions were systematically tested. Based on the typical ionic composition in natural waters (Na^+, Ca^{2+}, CO_3^{2-}, SO_4^{2-}, PO_4^{3-}, *etc.*), a 200-fold concentration (20 mM) of interfering ions was added to the b-CDs solution containing 100 μM Fe^{3+} ($FeCl_3$ solution), respectively, and the fluorescence spectra were measured (Fig. 10a). The results showed that cations (Na^+, Ca^{2+}) had a weak effect on the detected signals (fluorescence intensity fluctuation <10%). However, the presence of some anions (CO_3^{2-}, PO_4^{3-}) triggered a fluorescence enhancement, with the PL intensity being identical to that of DI water without any ions. It indicated that the anions (CO_3^{2-}, PO_4^{3-}) severely interfere with Fe^{3+} detection, leading to the failure detection of Fe^{3+} in solutions. This interference is likely due to the neutralization of anions and carboxyl or carbonyl groups on the surface of the b-CDs. SO_4^{2-} is a typical highly charged but structurally symmetric anion, and its tetrahedral configuration makes its coordination ability with carbon dot surface functional groups (*e.g.*, –COOH, –OH) significantly weaker than that of polydentate ligands (PO_4^{3-}), which makes it difficult to form complexes on the surface.[59] Therefore, it is not possible to trigger fluorescence enhancement or attenuation by neutralizing the charge or changing the surface state.

To assess the CD's performance in real-world conditions, we tested it with lake water samples from LaoYu Lake in Kunming, Yunnan, China. After filtering through a 0.22 μm membrane and centrifuging at 12 000 rpm for 20 minutes, the samples were spiked with Fe^{3+} at varying concentrations. As shown in Fig. 10b, the linearity of b-CDs for Fe^{3+} in natural water samples with diverse minerals and organic matter backgrounds was maintained (Fig. 10b, $R^2 = 0.99$). This result indicates that by calibrating the baseline signal, the developed sensor can reliably perform quantitative analysis of Fe^{3+} in real water environments.

4. Conclusions

In this study, multi-colored carbon dots (CDs) were successfully synthesized by controlling the acidic hydrothermal degradation of wheat bran and *o*-phenylenediamine under varying pH conditions. By adjusting the pH, CDs with distinct fluorescence properties—orange, green, and blue—were obtained, demonstrating that pH significantly influences the size, surface functional groups, and photoluminescence properties of CDs. The study reveals that the luminescence red-shift is primarily attributed to larger sp^2 domains, higher graphitization, and an increase in C=O functional groups, which collectively reduce the bandgap of the CDs. Furthermore, the potential application of these CDs in monitoring Fe^{3+} content in aquatic environments underscores their practical utility, the linear relationship predicted a detection limit of 378.76 nM for the prepared CDs with QY of 7.04%. This work not only advances the understanding of the luminescence mechanisms in carbon dots but also offers a simple yet effective strategy for tuning their photoluminescence properties through precursor degradation.

This study elucidates the synergistic mechanism of multi-color photoluminescence in wheat bran-derived carbon dots

and demonstrates their environmental sensing utility. In addition to the traditional focus on nitrogen doping in our study, we identify carbonyl (C=O) groups as contributors to the redshift of the emission. Combined with the sp^2 structural domain expansion (I_D/I_G reduced from 1.35 to 1.24), this dual tuning strategy was realized from 425 → 565 nm, providing a new design principle for wavelength-engineered CDs. On the other hand, by efficiently treating bran waste, our acid-conditioned hydrothermal method bypassed toxic reagents and successfully served as a Fe^{3+} sensor. Although resistant to cations (Na^+, Ca^{2+}), there were anion-induced false signals (*e.g.*, PO_4^{3-} interference leading to PL enhancement), which need to be optimally modified by surface ligand engineering at a later stage.

Data availability

Data will be made available on request.

Author contributions

Wenxuan Zheng: writing – review & editing, writing – original draft, conceptualization. Tianxiang Li: writing – review & editing, methodology. Yuhui Xie: supervision. Yadong Lv: supervision, writing – review & editing. Delong Xie: supervision, funding acquisition. Feng Wu: writing – review & editing, supervision, funding acquisition.

Conflicts of interest

There are no conflicts to declare.

Acknowledgements

The authors thanks the supporting by the National Natural Science Foundation of China (Grant No. 52403132 and 51603096), Yunnan Major Scientific and Technological Projects (No. 202302AG050002), Yunnan International Joint Laboratory of Sustainable Polymers (No. 202403AP140036), Yunnan Provincial Key Laboratory of Energy Saving in Phosphorus Chemical Engineering and New Phosphorus Materials (No. 202205AG070067), Yunnan Technological Innovation Center of Phosphorus Resources (No. 202305AK340002), and Engineering Research Center of Biodegradable Polymers, Educational Commission of Yunnan Province (No. KKPU202205001).

References

1 B. Lesiak, *et al.*, C sp2/sp3 hybridisations in carbon nanomaterials – XPS and (X)AES study, *Appl. Surf. Sci.*, 2018, **452**, 223–231.
2 Q. Wei, *et al.*, A novel hybrid sp-sp2 metallic carbon allotrope, *Front. Phys.*, 2018, **13**(5), 136105.
3 L.-M. Shen and J. Liu, New development in carbon quantum dots technical applications, *Talanta*, 2016, **156–157**, 245–256.
4 X. Xu, *et al.*, Electrophoretic Analysis and Purification of Fluorescent Single-Walled Carbon Nanotube Fragments, *J. Am. Chem. Soc.*, 2004, **126**(40), 12736–12737.
5 R. Das, R. Bandyopadhyay and P. Pramanik, Carbon quantum dots from natural resource: A review, *Mater. Today Chem.*, 2018, **8**, 96–109.
6 R. Jelinek, *Carbon-Dot Synthesis, in Carbon Quantum Dots: Synthesis, Properties and Applications*, ed. R. Jelinek, Springer International Publishing, Cham, 2017, pp. 5–27.
7 S. Y. Lim, W. Shen and Z. Gao, Carbon quantum dots and their applications, *Chem. Soc. Rev.*, 2015, **44**(1), 362–381.
8 Y. Liu, *et al.*, Primary Amine Functionalized Carbon Dots for Dead and Alive Bacterial Imaging, *Nanomaterials*, 2023, **13**(3), 437.
9 H. Ma, *et al.*, Synthesis and enhancement of carbon quantum dots from Mopan persimmons for Fe3+ sensing and anti-counterfeiting applications, *Chem. Eng. J.*, 2023, **453**, 139906.
10 P. Li, *et al.*, Waterborne fluorescent dual anti-counterfeiting ink based on Yb/Er-carbon quantum dots grafted with dialdehyde nano-fibrillated cellulose, *Carbohydr. Polym.*, 2020, **247**, 116721.
11 L. Li, *et al.*, Kilogram-Scale Synthesis and Functionalization of Carbon Dots for Superior Electrochemical Potassium Storage, *ACS Nano*, 2021, **15**(4), 6872–6885.
12 M. Jiang, *et al.*, Multicolor luminescence of carbon Dots: From mechanisms to applications, *Chem. Eng. J.*, 2024, **496**, 153761.
13 W. Cai, *et al.*, Full color carbon dots through surface engineering for constructing white light- emitting diodes, *J. Mater. Chem. C*, 2019, **7**(8), 2212–2218.
14 K. Zhao, *et al.*, Multi-color fluorescent carbon dots with single wavelength excitation for white light-emitting diodes, *J. Alloys Compd.*, 2019, **793**, 613–619.
15 H. Lv, *et al.*, Fluorescent cellulose-based hydrogel with carboxymethyl cellulose and carbon quantum dots for information storage and fluorescent anti-counterfeiting, *Cellulose*, 2022, **29**(11), 6193–6204.
16 S. Wang, *et al.*, Full-color biomass carbon dots for high-level information encryption and multi-color light emitting diode applications, *Microchim. Acta*, 2024, **191**(9), 538.
17 P. Li, *et al.*, Formation and Fluorescent Mechanism of Multiple Color Emissive Carbon Dots from o-Phenylenediamine, *Small*, 2024, **20**(29), 2310563.
18 Y. Ru, *et al.*, Rational Design of Multicolor-Emitting Chiral Carbonized Polymer Dots for Full-Color and White Circularly Polarized Luminescence, *Angew. Chem., Int. Ed.*, 2021, **60**(25), 14091–14099.
19 J. Jia, *et al.*, Synthesis of multicolor luminescent adjustable carbon dots and their application in anti-counterfeiting, *Mater. Today Chem.*, 2022, **25**, 100972.
20 Q. Zhao, *et al.*, Surface amino group modulation of carbon dots with blue, green and red emission as Cu2+ ion reversible detector, *Appl. Surf. Sci.*, 2022, **598**, 153892.
21 L. Jin, *et al.*, Orange-red, green, and blue fluorescence carbon dots for white light emitting diodes, *J. Mater. Sci. Technol.*, 2020, **50**, 184–191.

22 H. Zhang, *et al.*, Surface State-Based panchromatic luminescent carbon dots, *J. Colloid Interface Sci.*, 2025, **678**, 77–87.
23 J. Yu, *et al.*, Theoretical Understanding of Structure–Property Relationships in Luminescence of Carbon Dots, *J. Phys. Chem. Lett.*, 2021, **12**(32), 7671–7687.
24 Y. Zhou, *et al.*, Size-dependent photocatalytic activity of carbon dots with surface-state determined photoluminescence, *Appl. Catal., B*, 2019, **248**, 157–166.
25 T.-x. Li, *et al.*, Unraveling fluorescent mechanism of biomass-sourced carbon dots based on three major components: Cellulose, lignin, and protein, *Bioresour. Technol.*, 2024, **394**, 130268.
26 N. V. Tepliakov, *et al.*, sp2–sp3-Hybridized Atomic Domains Determine Optical Features of Carbon Dots, *ACS Nano*, 2019, **13**(9), 10737–10744.
27 J. Li, *et al.*, Luminescence color regulation of carbon quantum dots by surface modification, *J. Lumin.*, 2022, **246**, 118811.
28 Y. Song, *et al.*, Investigation from chemical structure to photoluminescent mechanism: a type of carbon dots from the pyrolysis of citric acid and an amine, *J. Mater. Chem. C*, 2015, **3**(23), 5976–5984.
29 S. Tao, *et al.*, Carbonized Polymer Dots: A Brand New Perspective to Recognize Luminescent Carbon-Based Nanomaterials, *J. Phys. Chem. Lett.*, 2019, **10**(17), 5182–5188.
30 F. Yan, *et al.*, Surface modification and chemical functionalization of carbon dots: a review, *Microchim. Acta*, 2018, **185**(9), 424.
31 K. Sato, *et al.*, Surface-Modified Carbon Dots with Improved Photoluminescence Quantum Yield for Color Conversion in White-Light-Emitting Diodes, *ACS Appl. Nano Mater.*, 2022, **5**(6), 7664–7669.
32 S. Maturi, *et al.*, Long-chain surface-modified red-emitting carbon dots as fluorescent additives for 3D printing vat-photopolymerization, *Nanoscale Adv.*, 2025, **7**(2), 448–455.
33 D. Benner, P. Yadav and D. Bhatia, Red emitting carbon dots: surface modifications and bioapplications, *Nanoscale Adv.*, 2023, **5**(17), 4337–4353.
34 T.-x. Li, *et al.*, Unraveling fluorescent mechanism of biomass-sourced carbon dots based on three major components: Cellulose, lignin, and protein, *Bioresour. Technol.*, 2024, **394**, 130268.
35 R. Dai, *et al.*, A pH-controlled synthetic route to violet, green, and orange fluorescent carbon dots for multicolor light-emitting diodes, *Chem. Eng. J.*, 2022, **431**, 134172.
36 B. Wang, *et al.*, Rational Design of Multi-Color-Emissive Carbon Dots in a Single Reaction System by Hydrothermal, *Advanced Science*, 2021, **8**(1), 2001453.
37 Y. Jiao, *et al.*, Novel Processing for Color-Tunable Luminescence Carbon Dots and Their Advantages in Biological Systems, *ACS Sustain. Chem. Eng.*, 2020, **8**(23), 8585–8592.
38 Y. Qiu, *et al.*, Carbon quantum dots derived from cassava stems via acid/alkali-assisted hydrothermal carbonization: formation, mechanism and application in drug release, *Ind. Crops Prod.*, 2023, **204**, 117243.
39 J. R. Bhamore, *et al.*, *Fluorescence sensing of Cu^{2+}ion and imaging of fungal cell by ultra-small fluorescent carbon dots derived from Acacia concinna seeds*, *Sens. Actuators, B*, 2018, **277**, 47–54.
40 M. A. Ahmad Farid, J. Lease and A. Yoshito, Lignocellulosic biomass-derived carbon quantum dots (CQDs): A novel approach utilizing organosolv lignin from Moso bamboo waste, *J. Cleaner Prod.*, 2024, **467**, 142852.
41 Y. Qiu, *et al.*, Green carbon quantum dots from sustainable lignocellulosic biomass and its application in the detection of Fe3+, *Cellulose*, 2022, **29**(1), 367–378.
42 L. Li and T. Dong, Photoluminescence tuning in carbon dots: surface passivation or/and functionalization, heteroatom doping, *J. Mater. Chem. C*, 2018, **6**(30), 7944–7970.
43 Y.-P. Sun, *et al.*, Quantum-Sized Carbon Dots for Bright and Colorful Photoluminescence, *J. Am. Chem. Soc.*, 2006, **128**(24), 7756–7757.
44 Z. Sun, *et al.*, Solvent-controlled synthesis strategy of multicolor emission carbon dots and its applications in sensing and light-emitting devices, *Nano Res.*, 2022, **15**(1), 414–422.
45 A. L. Matos, *Advances in the Synthesis of High-Quality Graphene by Hot-Filament Chemical Vapor Deposition Techniques and its Applications*, University of Puerto Rico, Rio Piedras (Puerto Rico), 2024.
46 A. Ferrari, S. Rodil and J. Robertson, Interpretation of infrared and Raman spectra of amorphous carbon nitrides, *Phys. Rev. B*, 2003, **67**(15), 155306.
47 A. C. Ferrari and J. Robertson, Interpretation of Raman spectra of disordered and amorphous carbon, *Phys. Rev. B:Condens. Matter Mater. Phys.*, 2000, **61**(20), 14095.
48 A. C. Ferrari and J. Robertson, Raman spectroscopy of amorphous, nanostructured, diamond–like carbon, and nanodiamond, *Philos. Trans. R. Soc., A*, 2004, **362**(1824), 2477–2512.
49 K. J. Mintz, *et al.*, A deep investigation into the structure of carbon dots, *Carbon*, 2021, **173**, 433–447.
50 J. Jia, *et al.*, Facile and Efficient Fabrication of Bandgap Tunable Carbon Quantum Dots Derived From Anthracite and Their Photoluminescence Properties, *Front. Chem.*, 2020, **28**(8), 123–133.
51 J. R. Lakowicz, *Principles of Fluorescence Spectroscopy*, Springer, 2006.
52 X. Wang, *et al.*, Bandgap-Like Strong Fluorescence in Functionalized Carbon Nanoparticles, *Angew. Chem., Int. Ed.*, 2010, **49**(31), 5310–5314.
53 C. Zheng, X. An and J. Gong, Novel pH sensitive N-doped carbon dots with both long fluorescence lifetime and high quantum yield, *RSC Adv.*, 2015, **5**(41), 32319–32322.
54 K. Hola, *et al.*, Photoluminescence effects of graphitic core size and surface functional groups in carbon dots: COO− induced red-shift emission, *Carbon*, 2014, **70**, 279–286.
55 S. V. Gaponenko, Optical Properties of Semiconductor Nanocrystals, *Cambridge Studies in Modern Optics*, Cambridge University Press, Cambridge, 1998.

56 M. Prückler, *et al.*, Wheat bran-based biorefinery 1: Composition of wheat bran and strategies of functionalization, *LWT–Food Sci. Technol.*, 2014, **56**(2), 211–221.
57 M. Reisinger, *et al.*, Wheat bran biorefinery – A detailed investigation on hydrothermal and enzymatic treatment, *Bioresour. Technol.*, 2013, **144**, 179–185.
58 J. J. G. C. van den Borne, *et al.*, Effects of pretreatment of wheat bran on the quality of protein-rich residue for animal feeding and on monosaccharide release for ethanol production, *Bioresour. Technol.*, 2012, **124**, 446–454.
59 J. Zhao, *et al.*, Anion coordination chemistry: From recognition to supramolecular assembly, *Coord. Chem. Rev.*, 2019, **378**, 415–444.